Acta Materialia 126 (2017) 221–235

Contents lists available at ScienceDirect

Acta Materialia

journal homepage: www.elsevier.com/locate/actamat

Full length article

Growth of {11$\bar{2}$2} twins in titanium: A combined experimental and modelling investigation of the local state of deformation

Y. Guo [a, c, *], H. Abdolvand [a, d], T.B. Britton [b], A.J. Wilkinson [a]

[a] Department of Materials, University of Oxford, Parks Road, Oxford, OX1 3PH, UK
[b] Department of Materials, Royal School of Mines, Imperial College London, London, SW7 2AZ, UK
[c] Laboratory for Mechanics of Materials and Nanostructures, Swiss Federal Laboratories for Materials Science and Technology (EMPA), 3602, Thun, Switzerland
[d] Department of Mechanical and Materials Engineering, Western University, London, Ontario, N6A 5B9, Canada

ARTICLE INFO

Article history:
Received 7 September 2016
Received in revised form
23 November 2016
Accepted 26 December 2016
Available online 28 December 2016

Keywords:
Deformation twinning
Local stress field
HR-EBSD
CPFE
Titanium

ABSTRACT

In this work we combine experiments and simulations to study the residual deformation state near twins in titanium at different stages of the complete twin growth process, including the twin tip: (i) far from a grain boundary, (ii) approaching a grain boundary, and (iii) intersecting with a grain boundary. High resolution electron backscatter diffraction (HR-EBSD) was used to characterise the local residual stress state and dislocation density distributions. Schmid factors were calculated from both the global deformation state (i.e. remote loading) and local deformation state (i.e. from high angular resolution EBSD). Crystal plasticity finite element modelling was used to simulate the stress field close to twins during loading and unloading. These simulations indicate that while the magnitudes of the localized stress fields close to twin boundaries are reduced upon removing the far field load, the major features of the stress fields in these regions are dominated by accommodation of the twin and thus persist from the peak load state to the unloaded state. We find a good correlation between the active twin variant and the maximum local Schmid factor, while the external loading (i.e. global Schmid factor) plays a less important role. These findings are useful in determining which twins will grow when a sample is deformed, and this has important implications for in service performance as well as texture evolution during mechanical processing.

1. Introduction

Deformation twinning is a very important and frequently occurring deformation mechanism in hexagonal close packed (HCP) metals [1]. Twin formation produces large shear within the crystal lattice [2] and the interaction of deformation twinning with grain boundaries can lead to damage nucleation [3]. For the HCP metals there are at least 7 types of twins [4], including 4 {$\bar{1}$01K} types and 3 {$\bar{2}$11K} types where K = 1, 2, 3, 4 for the former and 1, 2, 3, for the latter, and for each type there are 6 variants. These twin types can be initiated to accommodate contraction or extension strain along the <c> axis of the crystal, and whether a particular twin type is due to contraction or extension correlates with the c/a ratio of the material [5]. For titanium, with c/a ratio of ~1.588 [6], 4 types of twins are commonly observed [3,7] among which the {10$\bar{1}$2}<$\bar{1}$011> and {11$\bar{2}$1}<$\bar{1}$126> are extension twins and the {11$\bar{2}$2}<11$\bar{2}$3> and {10$\bar{1}$1}<10$\bar{1}$2> are contraction twins. The crystallographic relationships between these twins and their parents can be found in Ref. [7].

Nucleation of a twin could be associated with formation of zonal dislocations [8,9] by dissociation of lattice dislocations under suitable stress states [10]. Large bodies of research have treated twin nucleation as a critical resolved shear stress (CRSS) governed process [11–14] akin to the activation of dislocation sources. However, the viability of treating twin nucleation with Schmid factor criteria needs to be re-evaluated, as some investigations have discovered non-Schmid behaviour of twin nucleation [10,15–17]. The 'Schmid factor' referenced above is defined based on the external macroscopic loading, which we will refer to as 'Global Schmid factor (GSF)' in this work. This highlights that when a polycrystal is deformed, the local, i.e. microstructurally resolved,

* Corresponding author. Department of Materials, University of Oxford, Parks Road, Oxford, OX1 3PH, UK.
E-mail address: yi.guo@empa.ch (Y. Guo).

http://dx.doi.org/10.1016/j.actamat.2016.12.066

stress state can differ significantly from the external loading [18]. It is therefore necessary to probe the local stress state and relate the 'Local Schmid factor (LSF)' to the observed twin variant selection. Local stress measurement techniques that enable experimental evaluations of the LSF currently include: 3D-XRD [19], Differential Aperture X-ray Laue Micro-diffraction (DAXM) [20], High energy Transmission Laue Micro-diffraction (HETL) [21], and High (angular) Resolution EBSD (HR-EBSD) [22,23].

Wang et al. [24] and Abdolvand et al. [25–27] have statistically investigated the effect of stress heterogeneity on twin variant selection and stress partitioning between parent and twin crystals. Based on *in-situ* X-ray measurement of local stresses averaged over the parent grain they have suggested that LSF is the predominant factor influencing twin variant selection rather than GSF, and therefore CRSS criteria might still hold for the twinning process if it is to be assessed on a length scale local to the microstructural feature. However Wang et al. [24] point out that '*Stress close to the twin interface may be different from the grain-averaged stress*'. Apart from the local stress state at the twin-parent interface, the deformation compatibility across a grain boundary, i.e. the effects of neighbouring grains, have also been found to affect twin variant selection [16,28,29].

The process of twin growth has been classified as two steps by Yoo and Lee [5]: the lengthwise propagation along a twin shear direction, and the thickening process perpendicular to a twin invariant plane. The former is controlled by mobility of twinning dislocations [5] while the latter is dependent upon a continuous supply of zonal dislocation at the twin-parent interface [30]. The twin growth process is very fast and often has been treated as an instantaneous process [31]. Therefore, experimental characterisation of this process has rarely been reported. In this research we use HR-EBSD to capture the residual stress and GND density distribution (after removal of external loading) local to twin tips in different scenarios: (i) twins fully imbedded in the interior of a grain far away from any grain boundary, (ii) twins that have propagated across the grain interior and have tips near grain boundaries, and (iii) twins intersecting with grain boundaries. CPFE simulations are also performed to assess whether or not the residual stress field near the twin-parent interface in an unloaded specimen gives a reasonably interpretable indication of the nature of that stress field at peak loading.

2. Methodology

2.1. Experimental procedures

The material used in this research is Grade I commercial purity titanium (kindly supplied by Timet UK), the chemical composition of which is shown in Table 1.

Tensile test samples were cut from the as-received material using electron discharged machining followed by heat treatment at 830 °C for 24 h with furnace cooling to establish a grain size of ~300 μm with a low residual stress state (the geometry of these tensile samples has been reported elsewhere [6]).

The samples were then mechanically ground to 4000 grit followed by chemical mechanical polishing using colloidal silica (60 nm particle size) with intermittent etching using a solution consisting of 1% HF and 10% HNO_3 in water until a crisp grain shape was visible in optical microscopy under polarized illumination. The polished sample was deformed in tension to 1% plastic strain (~235 MPa), monitored using *in-situ* digital image correlation. The DIC was performed by marking both ends of the gauge section with high contrast markers whose displacements were tracked by a high speed camera mounted to the tensile testing rig (Shimadzu AGX-10 tensile testing machine). The sample was loaded at a cross-head displacement rate of 1 μm/s (7×10^{-5}/s strain rate) and then unloaded for HR-EBSD measurements. Various regions of interest featuring a twin tip in the interior of a grain, a twin tip near a grain boundary, and a twin tip intersecting with a grain boundary were scanned using a Zeiss Merlin FEG-SEM system and Bruker e-flash high resolution (1600 × 1200 pixels) EBSD detector. The working distance was 18 mm and scanning was performed using 14 nA beam current under 20 kV excitation voltage. At each beam position, a 1600 × 1200 pixel image of the diffraction pattern was captured with 1 s exposure time and stored as 12 bit images for offline analysis.

Table 1
Chemical composition of the as received Grade 1 commercially pure titanium.

Element	Fe	O_2	N_2	C	Ti
Composition	0.35 wt%	700 ppm	35 ppm	0.01 wt%	Balance

2.2. Elastic strain and GND density calculation from HR-EBSD

The strain and geometrically necessary dislocation (GND) density analysis are based on cross-correlating the diffraction patterns. In this process, a reference point was picked far away from the twin lath and toward the interior of the grain, where it was assumed that the stress was relatively low and uniform. For each diffraction pattern, 50 regions of interest (ROI) with 256 × 256 pixel size were selected with one at the middle of the pattern, 19 others surrounding it in a ring and the remaining 30 randomly distributed. These regions of interest on each of the test patterns were compared with the corresponding parts on the reference pattern [32] and their shifts were measured with a sensitivity of ~0.02 pixels [22]. These pattern shifts were used to fully determine the displacement gradient tensor (DGT) with the assumption that the normal stress perpendicular to the sample surface is zero [33]. Very often, lattice rotation local to some microstructure features, such as mechanical indents and deformation twins, can be very high (>10°), under such situations the elastic strain can no longer be accurately recovered due to large diffraction pattern shifts [23] and rotations. Therefore, it is necessary in the first step to estimate a finite rotation matrix from an initial diffraction pattern correlation and rotate the test pattern closer to the reference pattern. A second cross correlation analysis is then applied to the remapped pattern to determine the lattice strain [23]. The deformation gradient tensors from the first and second passes of cross correlation were combined to give a total deformation gradient $\boldsymbol{F}$ from which the Green strain tensor ($\boldsymbol{E}$) was obtained: $\boldsymbol{E} = 1/2(\boldsymbol{F}^{\boldsymbol{T}}\boldsymbol{F} - \boldsymbol{I})$. These elastic strain fields were then used to calculate stress fields using elastic constants (in GPa) for titanium: $C_{11} = 162.4$ $C_{33} = 180.7$ $C_{44} = 117$ $C_{66} = 35.2$ $C_{13} = 69.0$ [34]. Polar decomposition of $\boldsymbol{F}$ into the product of rotation and stretch tensors using singular value decomposition method enables the (finite) lattice rotation to be determined, which were used to estimate 2 in-plane spatial gradients for each of the 3 infinitesimal lattice rotations using procedures documented in Ref. [35] and linked to 6 out of 9° of freedom in Nye's dislocation tensor [36].

The GND density presented in this paper is a lower-bound estimation as 6 rotation gradients are used to recover 33 dislocation types for α-Ti: 3 <a> screw and 6 <c+a> screw; 3 <a> edge on basal plane; 3 <a> edge on first order prismatic plane; 6 <a> edge on first order pyramidal plane; 12 <c+a > edge on first order pyramidal plane [37]. In this GND analysis, there are more dislocation types than constraints from lattice curvature and so solution of the resulting equations is ambiguous. We proceed to make a lower bound estimate of GND densities using a standard linear

programming algorithm by minimizing the possible total GND line energy, accounting for edge and screw dislocation types and Burgers vector length [23], while necessarily supporting the measured lattice curvatures. The HR-EBSD analysis was performed using in-house developed Matlab code, the full function of which are now integrated into the commercial CrossCourt 4 software (blgvantage.com).

It is important to note that the absolute strain state of the reference pattern is unknown. Therefore the elastic strains presented here are relative values. The unknown stress at the reference point will affect the magnitude of local stress concentrations within the grain. However it will not affect the qualitative fact that the stress concentration exists. As far as possible, the reference points are placed away from microstructural features near which stress concentrations might be expected. This is also supported by the CPFE modelling presented in Section 3. However, note that uncertainty in the reference point stress state does not affect the GND density, as the GND density is only related with local lattice curvatures (i.e. spatial gradients of the rotation fields) [38].

2.3. Local and Global Schmid factor calculation

To reveal the effect of the local stress environment on the identified twin variant, the stress tensor local to the twin tip was used to obtain a 'Local Schmid Factor (LSF)', following the work of Abdolvand et al. [25,26]:

$$LSF = \frac{\boldsymbol{\sigma} : \boldsymbol{P}}{\|\boldsymbol{\sigma}\|} \tag{1}$$

where $\boldsymbol{\sigma}$ is the stress tensor mapped on global coordinates (sample surface) measured by HR-EBSD, $\boldsymbol{P}$ is the symmetric part of the tensor product of shear direction, $\boldsymbol{d}$, and shear plane normal, $\boldsymbol{n}$, which takes the following form:

$$\boldsymbol{P} = \frac{1}{2}\left[\begin{pmatrix} n_1d_1 & n_1d_2 & n_1d_3 \\ n_2d_1 & n_2d_2 & n_2d_3 \\ n_3d_1 & n_3d_2 & n_3d_3 \end{pmatrix} + \begin{pmatrix} n_1d_1 & n_2d_1 & n_3d_1 \\ n_1d_2 & n_2d_2 & n_3d_2 \\ n_1d_3 & n_2d_3 & n_3d_3 \end{pmatrix}\right] \tag{2}$$

The tensor $\boldsymbol{P}$ was populated for each interrogation point of the EBSD map using the local Euler angles and the identified twin shear direction and twin plane normal (using the coordinate systems established in Ref. [39]). The σ term is the highest normal stress component of the "diagonalised" stress tensor (absolute value of the highest principal stress). For a symmetrical matrix such as stress tensor, this is equal to the square root of the maximum Eigenvalue of the product between the stress tensor and its conjugate transpose. The calculated LSF takes into account both local stress tensor variations and orientation variations.

As a comparison, the Schmid factor obtained from external loading is termed 'Global Schmid Factor (GSF)', and is calculated using:

$$GSF = \frac{\boldsymbol{L}\cdot\boldsymbol{d}}{\boldsymbol{L}\cdot\boldsymbol{d}} * \frac{\boldsymbol{L}\cdot\boldsymbol{n}}{\boldsymbol{L}\cdot\boldsymbol{n}} \tag{3}$$

where $\boldsymbol{L}$ is the direction of the external loading.

2.4. CPFE modelling

As described in Section 2.1, all of the HR-EBSD measurements were carried out on an unloaded sample and this motivated a modelling study to relate these stress states back to the state of the sample under load as twin growth was occurring. Extensive details of the model used for this study are described elsewhere [40], but a brief description is provided here for completeness.

A user material subroutine (UMAT) was used to model twin reorientation and twin shear transfer, and their subsequent effects on the localized stress close to twin tips. In the UMAT, for each time increment, the total strain increment is provided by the ABAQUS finite element (FE) solver which can be used to calculate the total stress increment:

$$\Delta\varepsilon = \Delta\varepsilon^{el} + \Delta\varepsilon^{pl} + \Delta\varepsilon^{tr} \tag{4}$$

where $\Delta\varepsilon$ is the total strain increment given by the FE solver, $\Delta\varepsilon^{el}$ is the elastic strain increment, $\Delta\varepsilon^{pl}$ is the plastic strain increment as a result of slip, and $\Delta\varepsilon^{tr}$ is the transformation strain as a result of twinning. The rate of the plastic strain ($\dot{\varepsilon}^{pl}$) can be calculated using the following equation:

$$\begin{aligned} &\dot{\varepsilon}^{pl} = \sum_{\alpha=1}^{N^{spl}} P^{\alpha}\dot{\gamma}^{\alpha} \\ &P^{\alpha} = sym(S^{\alpha}) \ where \ S^{\alpha} = d^{\alpha} \otimes n^{\alpha} \end{aligned} \tag{5}$$

in which P^{α} is the symmetric part of the Schmid tensor (S^{α}) for the slip system α (detailed in Eq. (2)), and $\dot{\gamma}^{\alpha}$ is the shear rate on slip system α. A rate dependent equation is used for calculating the slip shear rates [41]:

$$\dot{\gamma}^{\alpha} = \dot{\gamma}_0 \left|\frac{\tau^{\alpha}}{g^{\alpha}}\right|^{n} sign\left(\frac{\tau^{\alpha}}{g^{\alpha}}\right) \tag{6}$$

where $\dot{\gamma}_0$ is a reference shear strain rate and n controls the rate dependency. τ^{α} and g^{α} are the resolved shear stress on the slip system α and strength of this system, respectively. In this study, it is assumed that prism, basal, and pyramidal slip systems are active deformation modes with the rate parameters of 0.001 and 50 assigned to $\dot{\gamma}_0$ and n [42]. The critical resolved shear stresses (g^{α} in Eq. (6)) for prism, basal, and pyramidal slips systems are assumed to be 70, 140, and 210 MPa, respectively, with no further hardening [43].

The twinning transformation strain ($\Delta\gamma^{tw}$) is applied incrementally during the transformation step (see below) within the pre-assigned twin domain until the characteristic twin shear for Ti (0.218) is fully achieved.

$$\begin{aligned} &\Delta\gamma^{tw} = \frac{0.218}{T_{TST}}\Delta t \\ &\Delta\varepsilon^{tr} = S^{tw}\Delta\gamma^{tw} \end{aligned} \tag{7}$$

where T_{TST} is the total time used for applying twin transformation strain and is assumed to be 3940 s to resemble quasi-static loading ($\dot{\varepsilon} = 5 \times 10^{-5}\ s^{-1}$). Δt is the time increment defined by the FE solver during each increment of transformation step, and S^{tw} is the twin variant Schmid factor. The time step is not meant to capture the real dynamic processes in the experiment but instead the twin transformation strain is increased relatively slowly to avoid numerical instabilities in the simulation.

A simplified abstraction of the grain geometry is used in which two grain boundaries perpendicular to the external loading axis separate three grains (see Fig. 1). The central layer is the parent grain which contains a predefined twin domain while the neighbouring grains in the two external layers do not twin. The grain orientations were assigned using the euler angles (Supplementary table 1) measured in the experiment.

These three central grains were surrounded by a boundary layer where a random orientation was assigned to each element in this layer (see Fig. 1). This is to reduce the effects of boundary conditions

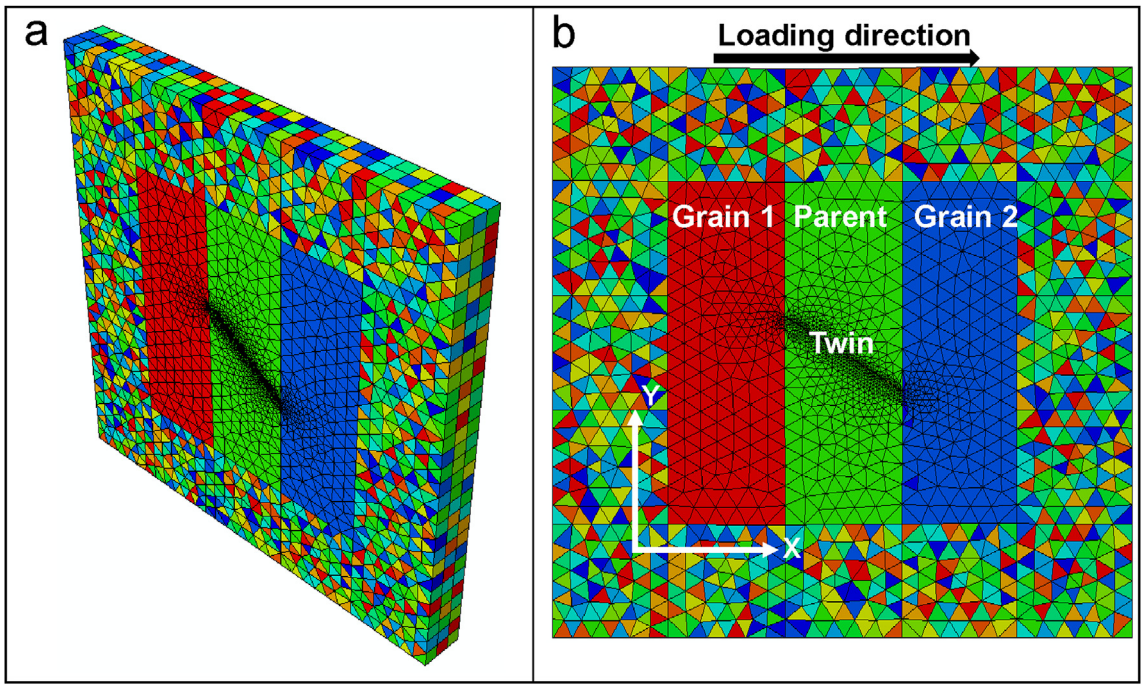

Fig. 1. Input model for simulating effects of unloading on the stress distribution (a) isometric view of the test-model (b) the model used to simulate measured grains.

on the stress development within the three central investigated grains.

A twin domain is embedded in the parent grain and is switched on once the plastic strain of $\varepsilon = 1\%$ has been applied. The applied boundary condition is symmetry x, y and z on the three external surfaces in the left, bottom and top of the model. Simulations are conducted in four steps. In step-1, a constant velocity is applied to the right hand side of the model (as shown in Fig. 1), in the x-direction, until $\varepsilon_{xx} = 1\%$ is reached. This strain is applied over the period of 600, i.e. at a similar strain rate to the experiment. The same orientation is assigned to the twin and parent domains for this step. In step-2, the twin domain is reoriented towards the twin orientations given in Table 2. In step-3, the transformation strain of 0.218 is applied to the twin domain (Eq. (7)). Both step-2 and step-3 are assumed to happen under constant applied strain. Steps 2 and 3 induce localized stresses close to the twin boundary in the parent and neighbouring grains, as a result of the accommodation of the twin transformation strain within these grains. After step-3, the model was unloaded and relaxed to compare the states of the calculated stresses for the loaded and unloaded cases.

3. Results

3.1. HR-EBSD measurements

In the current investigation, several instances of the $\{\bar{2}112\}[\bar{2}11\bar{3}]$ contraction twins were observed in different grains with twin tips far (>10 μm) away from a grain boundary, approaching a grain boundary, and fully intersecting a grain boundary. These features represent different stages of the contraction twin evolution and HR-EBSD results captured the differences in local, residual deformation fields associated with each stage of the twin evolution. The results are shown in Figs. 2–5, and the possible differences between the unloaded and loaded stress fields are discussed towards the end of Section 4. For all the images in Figs. 2–5, the loading direction is horizontal, i.e. along the x direction.

Table 2
Euler angles (in degrees) assigned to the modelled grain for different models.

Model	Grain 1	Parent	Twin	Grain 2
Fig. 2	[364, 49, 24]	[364, 49, 24]	[91, 34, 294]	[364, 49, 24]
Fig. 3	[336, 28, 5]	[336, 28, 5]	[86, 50, 270]	[336, 28, 5]
Fig. 5b	[344, 82, 36]	[195, 79, 188]	[261, 51, 96]	[32, 25, 326]

Fig. 2 demonstrates that from the surface observation, the twin is approximately 30 μm long and 2 μm wide and is fully imbedded within a grain and far away from the grain boundary. Crystallographic analysis of the misorientation between twin and parent shows that this twin is of contraction type with twinning plane $(\bar{1}\bar{1}22)$ and shear direction $<11\bar{2}3>$. Twin trace analysis also revealed that while the twin plane normal is always perpendicular to the long axis of the twin lath, the projection of the shear direction in the sample surface is generally not parallel to the long axis.

Increased GND density can be observed along the slip band intersecting the twin tip, indicating possible local interactions. The 2D projections of twin plane normal (Z_{twin}) and the twin shear direction (X_{twin}) are shown by the black arrows on the $\sigma^{twin}{}_{13}$ stress map, with dashed arrows indicating the direction pointing into the surface. The $\sigma^{twin}{}_{13}$ and $\sigma^{twin}{}_{33}$ represent the shear stress along the twin shear direction and the normal stress perpendicular to the twin plane, respectively. It can be seen that at both ends of the twin lath positive and negative stresses co-exist. The positive shear stress ($\sigma^{twin}{}_{13}$) is a necessary driving force for twin nucleation and propagation. This polarity of stress state can also be seen from the LSF maps, which show that the locations near the twin tip that have negative shear stress generally have a lower LSF and the places with positive shear stress have higher LSF.

Similar stress concentration around the tip of a propagating twin (approximately 3 μm wide and 100 μm long with the bottom end 20 μm from the grain boundary) can be observed for the same twin variant in a different grain as is shown in Fig. 3.

Similar to the previous case (Fig. 2), the regions of high GND density mainly concentrate at the twin tips and are significantly

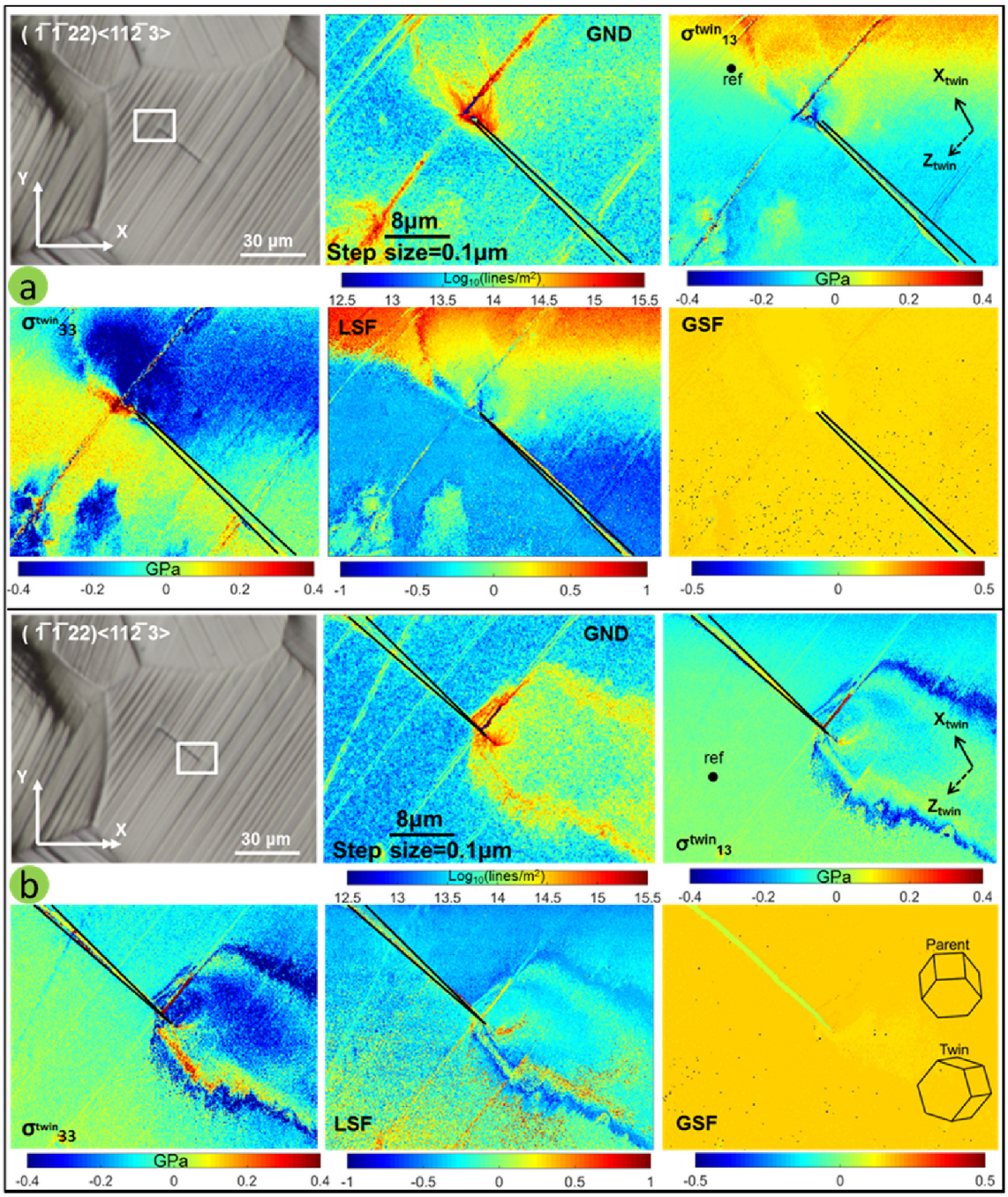

Fig. 2. Twin embedded in the interior of a large grain. Images in (a) and (b), from top left to bottom right are: optical image, GND density map, σ_{13}^{twin} stress map, σ_{13}^{twin} stress map, local Schmid factor map, and global Schmid factor map. Stress tensor components are those resolved onto twinning plane. 2D projection of the local coordinate system on the twin variant is indicated by X_{twin} (twin shear direction) and Z_{twin} (twin plane normal). The X and Y on the optical image indicate the sample coordinate system. The reference points used for cross correlation are indicated by the black dot on the σ_{13}^{twin} stress maps.

higher than at the twin-parent interface. The stress states change sharply across the twin lath at the twin tips, as revealed from both the $\sigma^{twin}{}_{13}$ and $\sigma^{twin}{}_{33}$ stress maps. The positive shear at both ends of the twin lath tends to provide a favourable condition for twin propagation, as revealed by the consistency between the position of highly positive LSF and $\sigma^{twin}{}_{13}$ shear stress around the twin tips. It can also be seen from the GSF map from Fig. 3 (a and b) that while the parent grain generally provides a favourable globally resolved shear stress (GSF~0.45) environment for this twin variant, the local deformation at one side of the tip tends to lower the globally resolved shear stress on the twin plane (indicated by the arrow). The shape of the region of lowered resolved shear stress (RSS) broadly converges with the shape of negative stress along both shear direction ($\sigma^{twin}{}_{13}$) and twin plane normal ($\sigma^{twin}{}_{33}$).

The twin shown in Fig. 4 is a $(2\bar{1}\bar{1}2)$ $<\bar{2}113>$ variant which is approximately 200 μm long and 5 μm wide as measured on the sample surface and spans across the parent grain with its tips located close to the grain boundaries. This twin is suspected to be reaching the end of the propagating phase and it shows a very different distribution of stress fields and dislocation density from

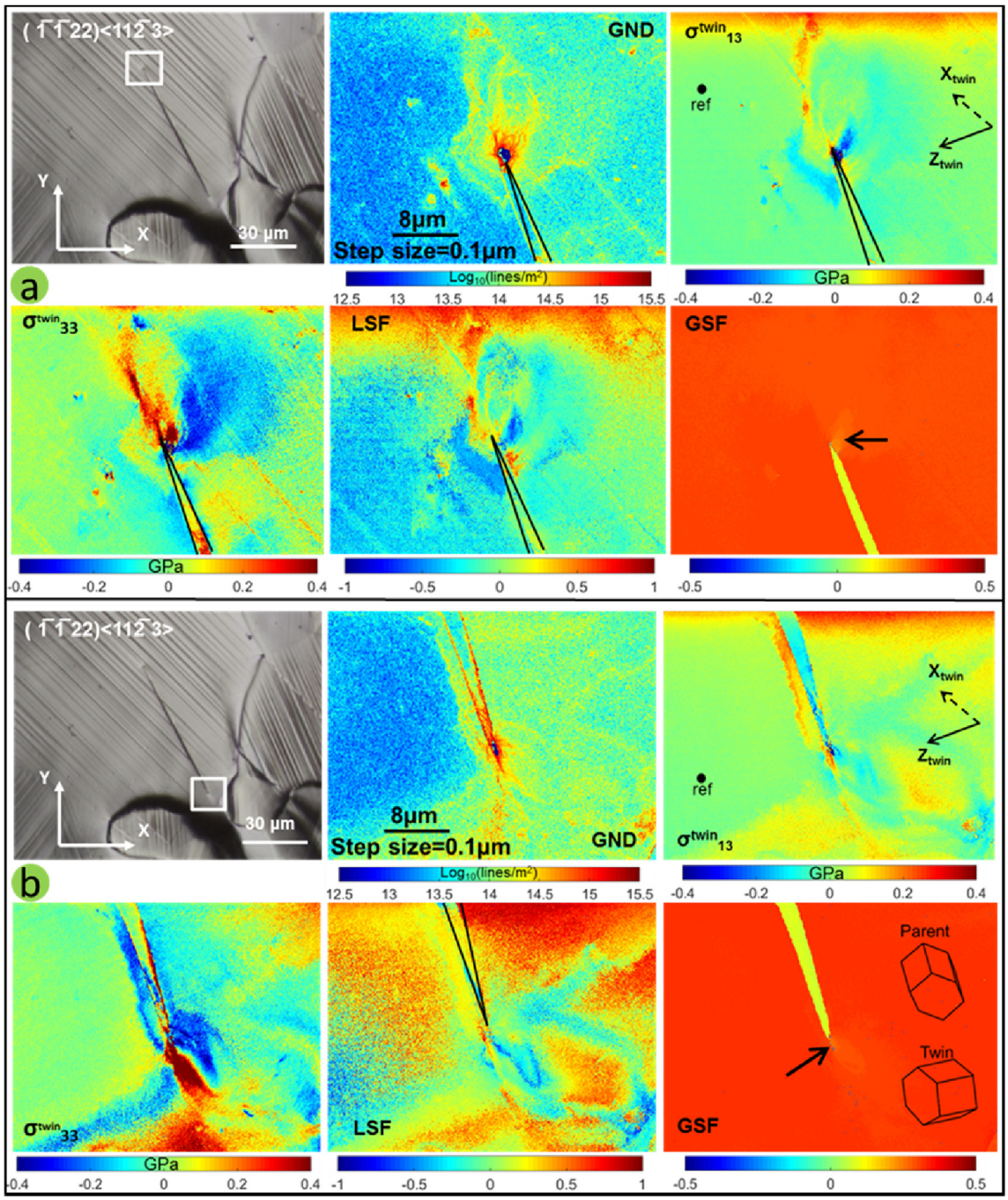

Fig. 3. Twin embedded in the interior of a large grain. Images in (a) and (b), from top left to bottom right, are optical image, GND density map, σ_{13}^{twin} stress map, σ_{13}^{twin} stress map, local Schmid factor map, and global Schmid factor map. Stress tensor components are those resolved onto twinning plane. 2D projection of the local coordinate system on the twin variant is indicated by X_{twin} (twin shear direction) and Z_{twin} (twin plane normal). X and Y on the first image indicate the global coordinate system. The reference points used for cross correlation are indicated by the black dot on the σ_{13}^{twin} stress maps.

the two cases illustrated in Figs. 2 and 3. The GND density and stress maps in Fig. 4b indicate that the majority of the deformation is confined within the twinning grain, while a limited amount of deformation is passed on to the neighbouring bottom grain. The neighbouring grain at the top, shown in Fig. 4(a), demonstrates a higher amount of deformation transfer, but mainly confined within the vicinity of the grain boundary. The negative-positive polarity of twinning shear is still observed at both ends of the twin lath, with positive shear mainly at the top right and bottom left side of the twin lath, while negative shear is evident at top left and bottom right. This is a fundamental change of the distribution of the stress field as well as the LSF condition (i.e. from mainly at the tip to mainly at the sides) as compared with Figs. 2 and 3 and suggests a change from mainly a propagation phase to mainly a thickening phase.

The difference between the cases shown in Fig. 5 (thickening stage) with the cases shown in Figs. 2–4 is that in Fig. 5 the twin tips are no longer sharp, which indicates that the twins have undergone adaptive growth along the grain boundary plane. The two twin and grain boundary interaction cases shown in Fig. 5 are from

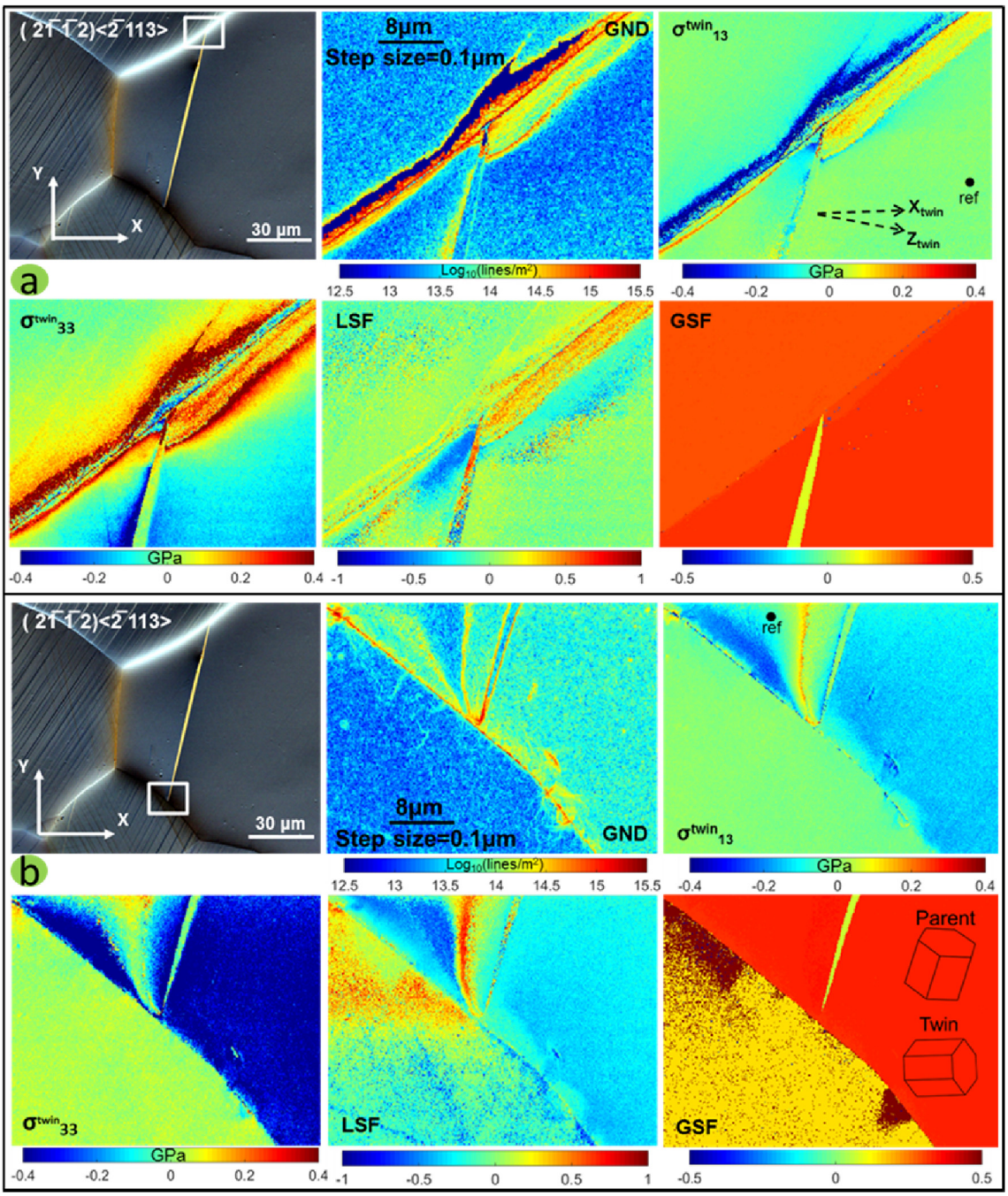

Fig. 4. Local deformation field at both ends of a twin that spans an entire grain. Images in (a) and (b), from top left to bottom right, are forward scattered electron image, GND density map, σ_{13}^{twin} stress map, σ_{13}^{twin} stress map, local Schmid factor map, and global Schmid factor map. Stress tensor components are those resolved onto twinning plane. 2D projection of the local coordinate system on the twin variant is indicated by X_{twin} (twin shear direction) and Z_{twin} (twin plane normal). X and Y on the first image indicate the global coordinate system. The reference points are indicated by the black dot on the σ_{13}^{twin} stress maps.

two different grains with Fig. 5 (a) demonstrating a twin tip propagation which is stopped by a grain boundary and just started the adaptive growth process, and Fig. 5(b) showing a twin tip that has widened significantly as evidenced from the width of the twin tip. Although there is no evidence indicating whether those twins nucleated from the grain boundary or from inside the grain, the deformation fields presented here reveal the general characteristic of twin-grain boundary interactions and are applicable to both scenarios. The twins shown in Fig. 5 have induced more significant deformation in the neighbouring grain, shown in the GND density and stress maps, as compared to the twin in Fig. 4 that is not fully interacting with the grain boundary. The amount of plasticity transfer appears to increase with the thickness of the twin lath as the thicker twin (Fig. 5(b)) has induced a larger GND density and in a wider spatial range compared with the thinner twin (Fig. 5(a)). The shear stress ($\sigma^{twin}{}_{13}$) maps show remarkable similarity with those demonstrated in Fig. 4 as the positive shear stress concentrates on one side of the twin tips while on the other side there is mainly negative shear stress. This observation is however different from the cases shown in Figs. 2 and 3, where the stress fields at the

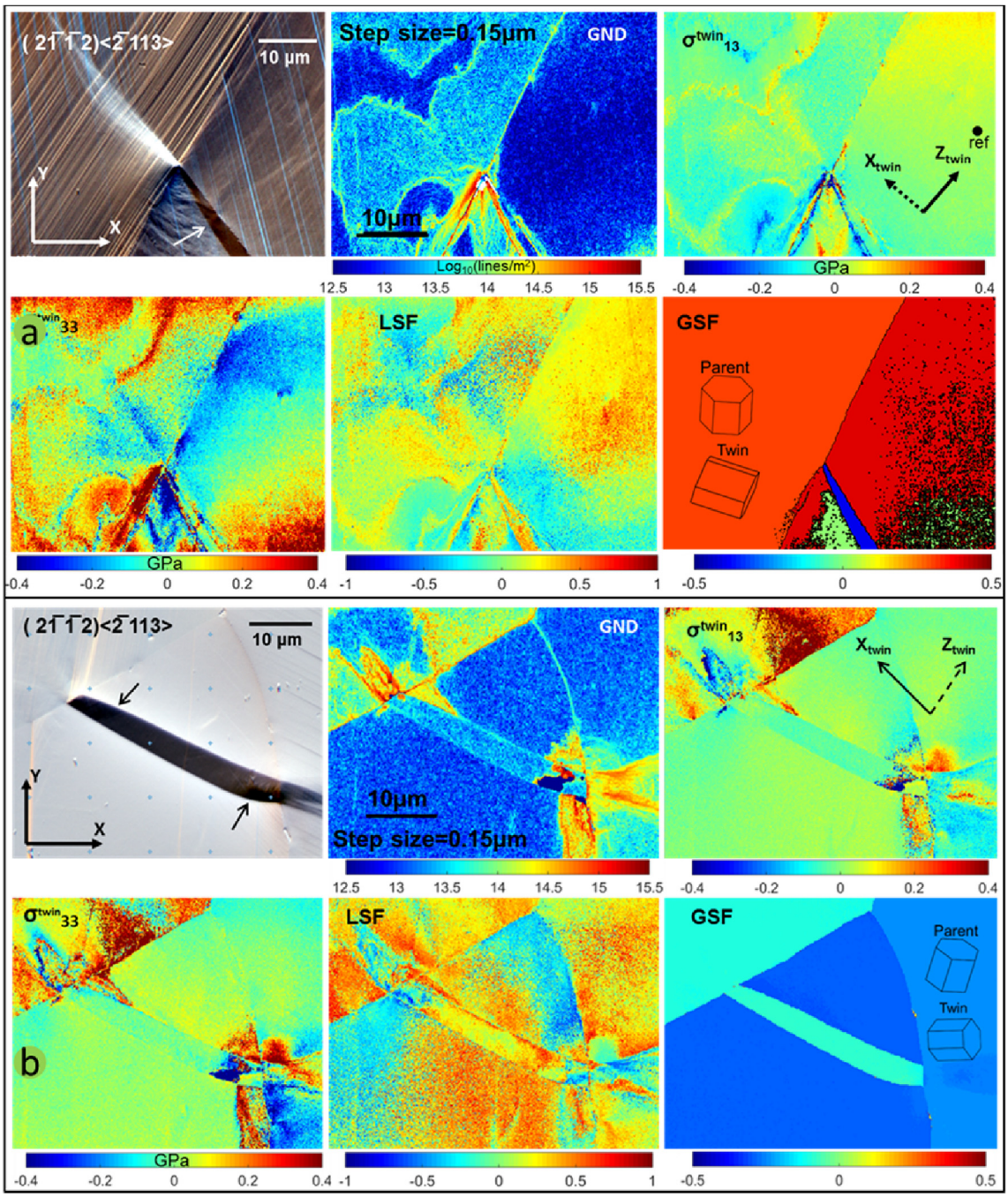

Fig. 5. Twin tip interactions with grain boundaries. Images in (a) and (b), from top left to bottom right, are fore-scattered electron image, GND density map, σ^{twin}_{13} stress map, σ^{twin}_{13} stress map, local Schmid factor map, and global Schmid factor map. Stress tensor components are those resolved onto twinning plane. 2D projection of the local coordinate system on the twin variant is indicated by X_{twin} (twin shear direction) and Z_{twin} (twin plane normal). X and Y on the first image indicate the global coordinate system. The reference points used for cross correlation are indicated by the crosshair on the stress maps.

twin tips are less affected by the grain boundary. This difference also suggests that the change in stress and LSF distribution at the twin-parent interface near the twin tip is an indicator of different phases of twin growth.

3.2. CPFE simulations

The results of the simulations outlined in Table 2 are presented in Fig. 6.

Grain orientations studied experimentally in Figs. 2, 3 and 5b were modelled. Experimentally, the twins were fully embedded in their corresponding parent grains for Figs. 2 and 3, hence all three simulated grains shown in Fig. 6a and (b) were given the same orientation as the parent grain, so that there were initially no grain boundaries. However, the twin was restricted to the central layer. In the first column of Fig. 6, the calculated in-plane stresses at the end of the loading step are shown. At the end of the twin shear transfer step (column 2), the formation of the twin induced a localized stress field in the three grains which are much greater in magnitude than the stresses caused by the external loading. These intense

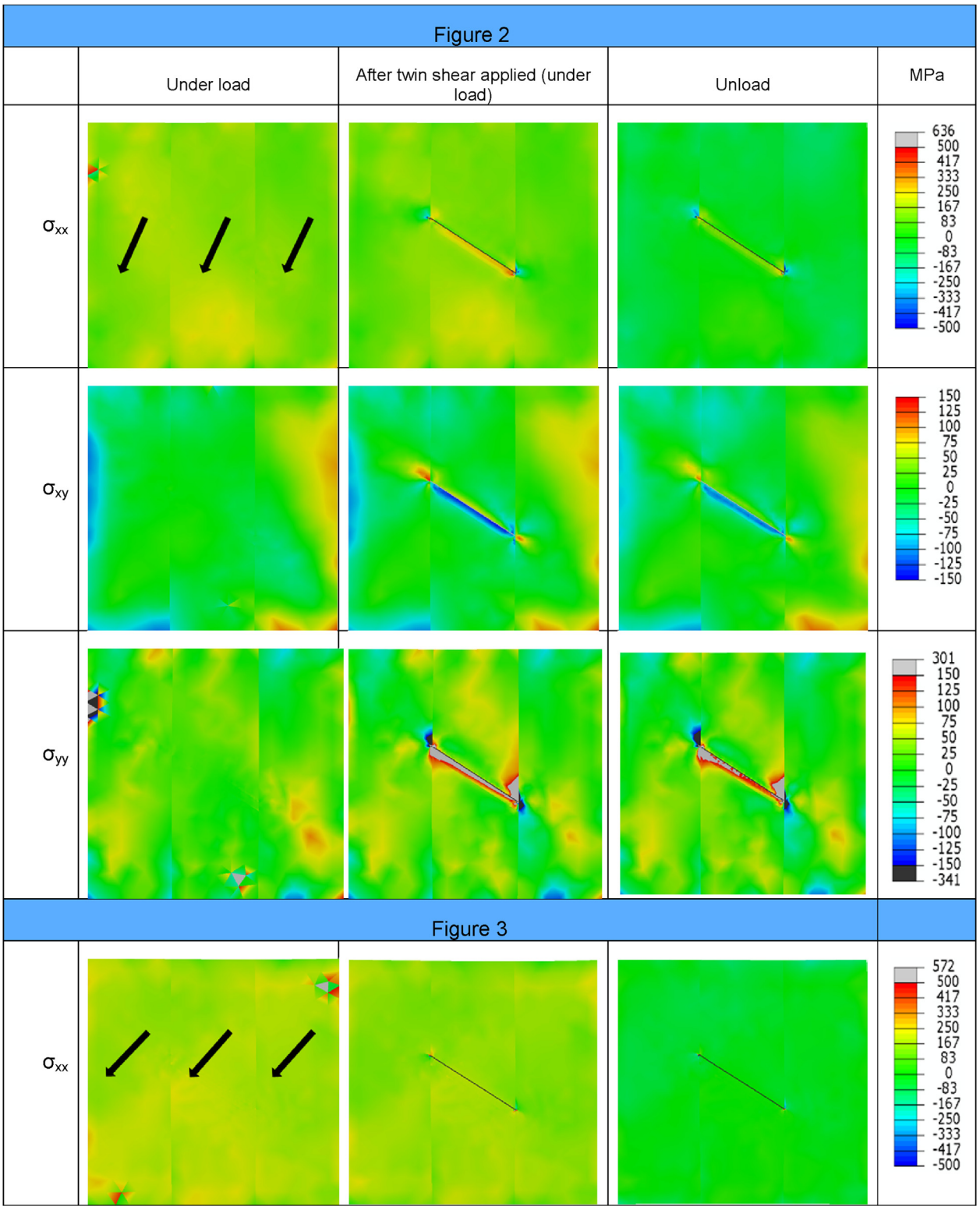

Fig. 6. Evolution of the in-plane stress components for three measured cases: Figs. 1, 2 and 5b. Stresses are calculated at the end of the loading step ($\varepsilon = 1\%$), at the end of the twin shear transfer step (under load), and at the end of the unloading step. Arrows in σ_{xx} figures represent the direction of the c-axis of the HCP crystal and load is applied along the x-direction.

localized stress variations caused by the twin do not vanish upon unloading (column 3), although their magnitudes are somewhat reduced. These trends are also seen for the other two model-cases of the experimental data, Figs. 3 and 5(b). In the case of Fig. 5(b), there is more stress variation before twin insertion due to the anisotropy of the elastic and slip responses of the different grain orientations. The average stresses in (i) the whole model, and (ii) the twin and parent grains at the end of loading, twin shear

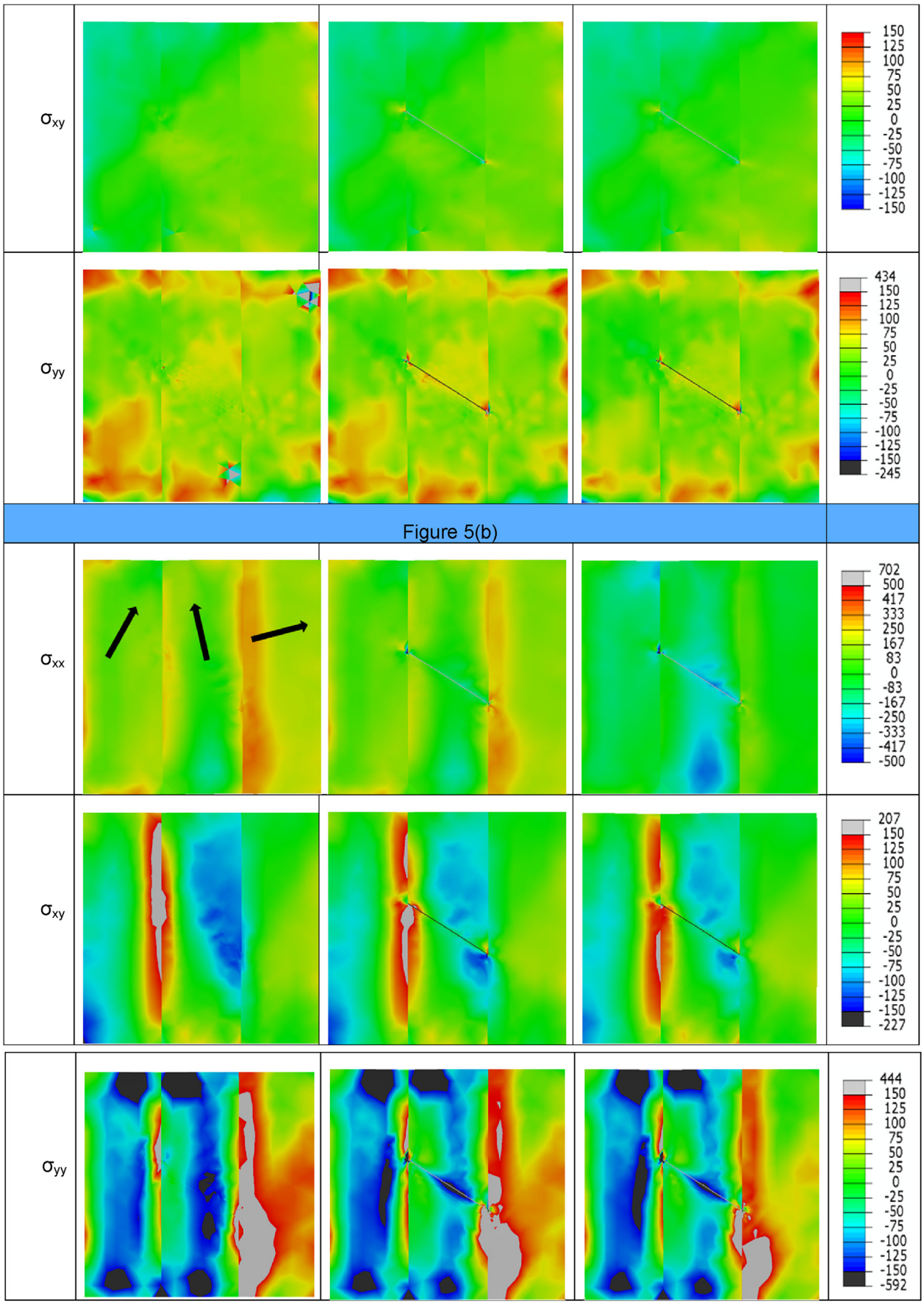

Fig. 6. (*continued*).

transfer, and unloading stages are shown in Table 3. For all of these cases, it can be seen that the pattern of stress variation is dominated by the insertion of the twin domain rather than by the external loading and that this pattern persists on unloading. Unloading causes only a minor change in the magnitudes of the calculated stresses. Three extreme scenarios of deformations are also modelled in order to gain a more generalized view of the stress relaxation process, including a single crystal case where c axis of the grain is perpendicular to the external loading direction, one case where the c axis of the neighbouring grains are perpendicular to the c axis of the twinning grain, and one case where the c axis of the neighbouring grains are at 45° to the twinning grain. The results are shown in the supplementary (Supplementary Fig. 1 and Supplementary Table 2) and they show that while unloading leads to various degree of stress relaxation, no sign reversal is observed. Therefore, from the modelling results, it is reasonable to conclude that the stress fields we measure after unloading are qualitatively representative of those under load.

4. Discussion

4.1. Local deformations around the twin tips

Contraction twinning activated by tensile loading has been characterised in CP-Ti using HR-EBSD at different phases of twin growth, i.e. during propagation, near a grain boundary, and interacting with grain boundary. The convenience of accessing local stress tensors at the submicron length scale makes HR-EBSD a powerful tool to study deformation heterogeneity in crystalline materials. In this study, stress fields on the sample surface in the global coordinate system were captured by HR-EBSD. These were rotated onto the habit plane and shear direction of the active twin variant in order to investigate the twinning shear during the twin growth process. In addition, the local stress tensor at each interrogation point was also combined with the corresponding orientation matrix to generate a local Schmid factor which indicates the extent to which the local stress tensor is dominated by the resolved shear stress on the activated twin variant within the parent matrix grain. Figs. 2 and 3 demonstrate the elongation dominated twinning process as the twinned crystal maintains a high aspect ratio. The case shown in Fig. 4 represents a transition from the elongation dominated phase to a thickening dominated phase, and the cases shown in Fig. 5 represent a thickening dominated phase of the twinning process.

At the twin elongation phase, illustrated in Figs. 2 and 3, stress concentration is significantly focused at the twin tip and radiates out along the twin shear direction. The stress concentration is found to change from positive to negative across the twin lath and near the twin tips, and this polarity is reflected also within the distribution of the LSF. Furthermore, the twin variant activation is highly correlated with RSS [44], but, unlike dislocation slip, twinning is only possible in the positive shear direction [2]. Therefore, the local positive shear directly in front of the twin tips supports continued twin propagation across the parent grain even when the global Schmid factor does not favour twin propagation in some cases. A common feature demonstrated in Figs. 2 and 3 is that positive twinning shear mainly concentrates in front of the twin tip, while negative shear is found mainly at the twin-parent interface near the tip. This feature possibly results from the large shear strain required to create the twin domain and the force equilibrium requirement across the twin-parent interface. The presence of such a negative shear field and the high GND concentration at the twin tip are very likely the reasons the twins stop elongating at 1% external strain. In order for the twins to continue lengthwise growth, a higher external load would need to be applied. The observed stress field distribution is broadly consistent with the recent modelling work [45]. However, the magnitude of twin shear observed experimentally here in Ti is much higher than for the softer Mg case considered by the modelling in Ref. [40].

When approaching a grain boundary, the stress field at the twin tip changes dramatically as the compatibility of the neighbouring grain also begins to have a significant effect, in addition to the compatibility with the parent grain. Both high shear stress ($\sigma^{twin}{}_{13}$) and high normal stress ($\sigma^{twin}{}_{33}$) were found to distribute at the twin tip and along the twin lath and grain boundary. The local positive shear and positive LSF near the twin tip were no longer found to concentrate directly in front of the twin tip. Instead, they radiate out from the twin front sideways into the surrounding matrix, as can be seen in Figs. 4 and 5, which is probably affected by the neighbouring grain orientation and grain boundary geometry. This change of shear stress distribution and LSF environment seems to indicate a change in the twin driving force from propagation to thickening.

In both the propagating and thickening stages, the LSF does not apparently provide a long range field that affects large portions of the twin lath, rather, there exists only a small window of favourable LSF field around the twin tip. This is possibly due to the exhaustion of driving force in the thickened mid-section of the twin lath, and indicates that twin propagation and thickening is a highly localized event. Moreover, significantly higher GND density concentration can be found at the twin tip region compared to the twin lath, as is directly evidenced by the GND maps in Figs. 2–5. From these figures it is clear that twinning-related local plasticity occurred mainly at the twin tip rather than the whole lath, therefore the twinning process is likely to be a 'tip-controlled' mechanism. It is interesting to see from Fig. 5 that for twin tips intersecting a grain boundary, the GND density distribution is one sided, for example in Fig. 5(b) the GND concentration can be seen mainly at the top side on the right end and at the bottom side on the left end of the twin lath. These sites are also where the highly positive shear and LSF are located. These features serve as evidence to the possibility that the twin growth is one-sided at both ends of the twin tips, at least for the cases shown in Fig. 5. This one-sided growth leads to the observed curvatures near the tip of the twin as indicated by the arrows in the SEM images in Fig. 5.

For a twin tip near a grain boundary, stress may or may not be induced in the neighbouring grain as can be seen in Fig. 4. This depends on several factors. The most obvious factor is the distance of the twin tip from the grain boundary and the decay of the stress field ahead of the twin tip. An example of this is seen in Fig. 4, in which one twin tip is approximately 1 μm from the grain boundary

Table 3
The average stress in the whole model and in the parent and twin at (a) the end of loading, (b) the end of shear transfer, and (c) the end of unloading.

Average Stress	For the whole model (MPa)			Averaged over parent and twin (MPa)		
	σ_{xx}	σ_{yy}	σ_{xy}	σ_{xx}	σ_{yy}	σ_{xy}
(a) At the end of loading (1% plastic strain)						
Fig. 1	225.7	0	0	166.5	24.9	−8.4
Fig. 2	232	0	0	186.6	49.8	16.3
Fig. 5b	233	0	0	182.9	−24.4	−10.5
(b) At the end of Twin Shear Transfer (constant applied strain)						
Fig. 1	184.2	0	0	127.1	24.3	−3.2
Fig. 2	197.8	0	0	157.1	45.1	14
Fig. 5b	198.4	0	0	156	8.3	−11.8
(c) At the end of unload						
Fig. 2	0	0	0	−45.8	18.7	−1
Fig. 3	0	0	0	−30.6	37.1	6.6
Fig. 5b	0	0	0	−36.2	16.2	−10.5

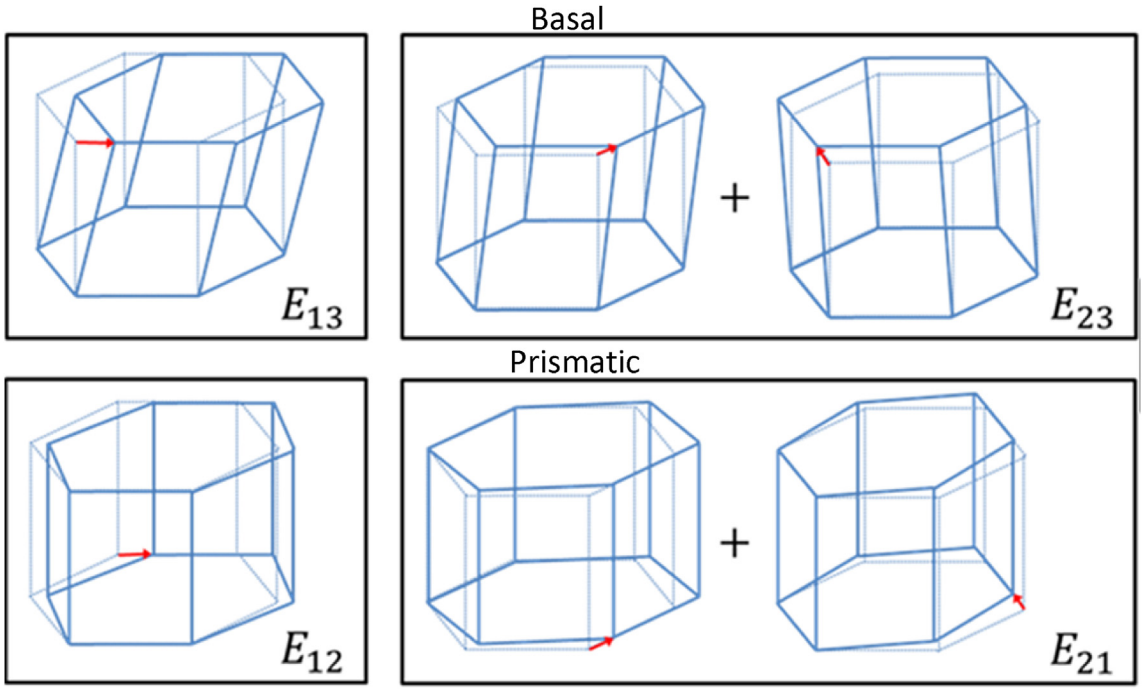

Fig. 7. Physical interpretation of the displacement gradient tensor components and the related shear displacement, highlighted with a red arrow, on crystallographic planes. (For interpretation of the references to colour in this figure legend, the reader is referred to the web version of this article.)

(Fig. 4(b)) and no obvious deformation can be seen in the neighbouring grain, while the other end of the twin tip is actually intersecting the grain boundary (Fig. 4(a)) and has induced deformation in the neighbouring grain. Another factor is that the twin shear direction (as indicated by the dashed arrow X_{twin} on the σ_{13}^{twin} map in Fig. 4) in this case does not have a significant resolved component perpendicular to the grain boundary plane. This effect also influences the top twin tip in Fig. 4(a) which is interacting with the grain boundary, in which case there is a large shear component along the grain boundary plane rather than perpendicular to it and the stress field is smeared along the grain boundary plane rather than extended into the interior of the neighbouring grain.

The capability of the neighbouring grain to accommodate twinning shear was assessed by Qin and Jonas [16,28]. In principle, this method works by first rotating the twin shear displacement gradient tensor $\begin{pmatrix} 0 & 0 & t \\ 0 & 0 & 0 \\ 0 & 0 & 0 \end{pmatrix}$ (t is twinning shear and t = 0.218 for $\{11\bar{2}\,2\}$ contraction twins in titanium), as defined in the twin local coordinate system, into the orientation of the neighbouring grain. When this is done for the case reported in Fig. 4, the displacement gradient tensors in the top and bottom grains take the form of

$$E_{top} = \begin{pmatrix} -0.0902 & 0.0437 & -0.0524 \\ -0.1445 & 0.0700 & -0.0839 \\ 0.0349 & -0.0169 & 0.0203 \end{pmatrix}$$

and

$$E_{bottom} = \begin{pmatrix} -0.0115 & -0.0100 & 0.0002 \\ 0.0163 & 0.0143 & -0.0003 \\ 0.1630 & 0.1423 & -0.0028 \end{pmatrix}$$

Assuming a crystal Cartesian reference frame on a crystal orientation is defined such that the X direction is consistent with the $<11\bar{2}\,0>$ Burgers vector direction and the Z direction is the basal plane normal direction, the rotated displacement gradient tensor should have $|E_{12}| + |E_{21}|$ representing the amount of shear that can be accommodated by prismatic slips, $|E_{13}| + |E_{23}|$ the amount of shear that can be accommodated by basal slips, as is graphically illustrated in Fig. 7. The more difficult twinning or <c+a> pyramidal slip modes are linked to components of $\boldsymbol{E}$ involving displacement along the X_3 axis (i.e. $|E_{31}| + |E_{32}|$) that cannot be achieved by the easier <a> slip systems.

The $|E_{12}| + |E_{21}|$ was found to be 0.188 for the top grain and 0.026 for the bottom grain and the $|E_{13}| + |E_{23}|$ is 0.136 for the top grain and 0.001 for the bottom grain. Therefore the top grain is 'softer' and the bottom grain is 'harder' in terms of accommodating the twining shear through prismatic and basal dislocation slips (which have lower critical resolved shear stress for CP-Ti [43]). This might help explain the less well-developed deformation field in the bottom grain (Fig. 4(b)) compared with the top grain (Fig. 4(a)), as revealed by both the GND and the stress maps.

In order to assess the role of resolved shear stress on twin variant selection, the LSF and GSF for all six variants of the above shown twin cases are calculated and the results are shown in Fig. 8.

It can be seen that for twins far away from a grain boundary (Figs. 2 and 3) the active twin variant has the highest LSF among all possible variants but their GSFs are comparatively low. The twin shown in Fig. 2(a) may not have the highest LSF, but its magnitude is close to the highest, and the local stress concentration might have been modified slightly by interactions with the slip bands. For the cases where the twin is very close to or intersecting with the grain boundary, Figs. 4 and 5, neither their LSF nor GSF are the highest among all possible variants. These results seem to indicate that while a twin is far away from a grain boundary, it is the local stress field that directly influences twin propagation rather than the externally applied stress. When the twin extends to the grain boundary, the activated twin variant is no longer favoured by the local stress field, possibly due to the presence of the neighbouring grain and grain boundary. Under such conditions, the twin would either grow thicker under a continuous increase of the external

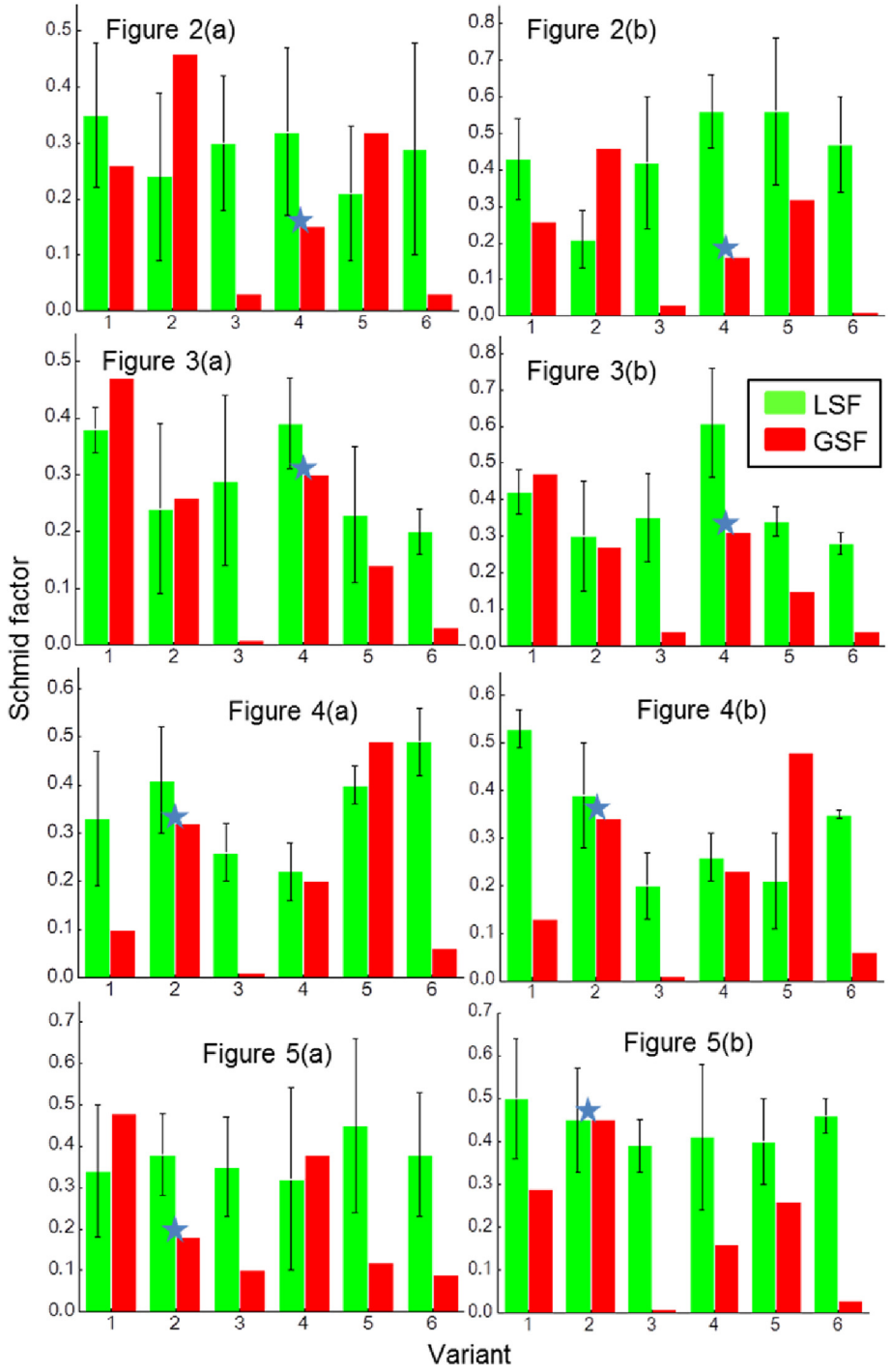

Fig. 8. LSF and GSF of all 6 twin variants for the twin cases examined. Activated twin variants are indicated by stars.

macroscopic strain, where the deformation in the neighbouring grain may modify the local stress state at the twin tip, or other twin variants with the highest LSF are nucleated from the twin-grain boundary interactions. This observation is supported by the pioneering *in-situ* TEM work on twin mechanisms by Jin and Bieler [46].

4.2. Evolution of stress during the unload step

The observations in this research are *ex-situ* after unloading, therefore the stresses for the twin tips are residual and provide a first order ranking of the applied stress state. The mechanical deformation was a maximum tensile strain of 1%, which corresponds to a maximum tensile stress of 235 MPa. Thus, on average, the σ_{11}^{global} values are ~235 MPa lower in the residual stress maps than they would have been at the peak load. A preliminary estimate is to assume that the unloading caused a uniform elastic reduction in the stresses. The shear stress σ_{13}^{twin} at peak load would then need to be at most $235/2 = 118$ MPa higher than the measured residual values. A better estimation can be made by using the GSF values in

combination with the 235 MPa peak stress. In Fig. 2 the GSF is ~0.25 in the parent grain, giving only a ~59 MPa contribution to σ_{13}^{twin} (from the external peak load), which is smaller than the residual stress contributions reported in the key locations near the twin and therefore this *ex-situ* observation should not deviate significantly from the *in-situ* condition. Similarly, for Fig. 3 the GSF is ~0.4 corresponding to a σ_{13}^{twin} of ~95 MPa, while the residual stress is again rather larger than this (~×2) in the key regions. For the other cases considered a similar situation emerges in which the residual σ_{13}^{twin} values in the stress concentration regions close to the twins are of larger magnitude than those expected from the average externally applied peak stress. Therefore, the qualitative interpretation of the residual stress fields should essentially remain unaltered from the loaded condition.

A better assessment of the effect of unloading was achieved using a crystal plasticity finite element (CPFE) model. This takes into account the relaxation process during unloading, allowing the stress reduction to be spatially varying, and allowing local plastic deformation through slip if the yield condition is exceeded locally. Studying the effects of each assumption made in the twin shear transfer model on the state of the calculated values is beyond the scope of this present paper, and indeed these effects are discussed in detail elsewhere [40]. Although unloading does induce stress reversal at a grain averaged level as can be seen, for example σ_{yy}, from Table 3, this does not affect the stress concentration close to the twin lath, which is clearly demonstrated by the results in Fig. 6. The reason for the reversal of sign in the grain average stress field lies in the stress state inside the twin [40]. The pattern of residual stresses found near the twins in the parent (and neighbouring) grains, which are what we focus on in this investigation, captures well the situation that was present at peak loading and is not qualitatively affected by the unloading process.

5. Conclusion

Different stages of the twin growth process were characterised using HR-EBSD. This study focused on the $\{11\bar{2}\,2\}$ contraction twin variants nucleated in grain interiors and progressing to interact with grain boundaries. Based on the HR-EBSD stress maps and LSF field calculations, supported by CP-FEA modelling, the following conclusions may be drawn:

1. During the propagation stage, both positive and negative shear stress concentrations can be found at the twin tips. The positive stress field concentrates directly in front of the twin tip and creates a favourable LSF condition for twin extension. A negative stress field concentrates at the edge of the twin front and tends to resist the twin elongation. The negative shear together with high GND concentration at the twin tip serve as barriers for twin propagation.
2. As a twin approaches a grain boundary, the local stress state changes dramatically and the positive shear stress is no longer found directly in front of the twin tip. Rather, a small window of positive shear stress and favourable LSF condition affecting only a small portion of the twin tip can be found at the edge of the twin lath, and it radiates sideways into the matrix. This indicates that the twinning process shifted from an elongation dominated process to a thickening dominated process at the grain boundary.
3. Resolved shear stress as computed from far-field external loading is not reliable for analysing twin variant selection. The resolved shear stress based on the local stress tensor and lattice orientation at the immediate twin environment is needed for better twin variant prediction.
4. Deformation compatibility requirements across grain boundaries could affect the local stress field at the twin tip and other twin variants might be favoured over the current twin variant near the grain boundary.

Acknowledgements

We acknowledge funding from the EPSRC within the HexMat programme grant (EP/K034332/1). TBB acknowledges funding for his research fellowship from the Royal Academy of Engineering. We thank Dr. Aimo Winkelman for helpful discussions concerning the description of Euler angles within the Bruker EBSD software. We thank Dr. Mikhail Polyakov for proof reading the manuscript. Data supporting this manuscript are available on the Oxford Data Archive (http://ora.ox.ac.uk/).

Appendix A. Supplementary data

Supplementary data related to this article can be found at http://dx.doi.org/10.1016/j.actamat.2016.12.066.

References

[1] T.B. Britton, F.P.E. Dunne, A.J. Wilkinson, On the mechanistic basis of deformation at the microscale in hexagonal close-packed metals, Proc. R. Soc. Lond. A Math. Phys. Eng. Sci. 471 (2015). http://rspa.royalsocietypublishing.org/content/471/2178/20140881.abstract.
[2] J.W. Christian, S. Mahajan, Deformation twinning, Prog. Mater. Sci. 39 (2000) 1–157.
[3] M.H. Yoo, Slip, twinning, and fracture in hexagonal close-packed metals, Metall. Mater. Trans. A 12A (1981) 409–418.
[4] S. Mendelson, Zonal dislocations and twin lamellae in h.c.p. metals, Mater. Sci. Eng. 4 (1969) 231–242, http://dx.doi.org/10.1016/0025-5416(69)90067-6.
[5] M.H. Yoo, J.K. Lee, Deformation twinning in h.c.p. metals and alloys, Philos. Mag. A 63 (1991) 987–1000.
[6] Y. Guo, D.M. Collins, E. Tarleton, F. Hofmann, J. Tischler, W. Liu, R. Xu, A.J. Wilkinson, T.B. Britton, Measurements of stress fields near a grain boundary: exploring blocked arrays of dislocations in 3D, Acta Mater. 96 (2015) 229–236, http://dx.doi.org/10.1016/j.actamat.2015.05.041.
[7] L. Wang, Y. Yang, P. Eisenlohr, T.R. Bieler, M.A. Crimp, D.E. Mason, Twin nucleation by slip transfer across gran boundaries in commercial purity titanium, Metall. Mater. Trans. A 41A (2010) 421–430.
[8] M.L. Kronberg, Atom movements and dislocation structures for plastic slip in single crystals of β-uranium, J. Nucl. Mater. 1 (1959) 85–95, http://dx.doi.org/10.1016/0022-3115(59)90013-3.
[9] S. Mendelson, On zonal dislocation and their origin for twinning and martensite formation, in: J. Perkins (Ed.), Shape Menory Eff. Alloy, Springer US, 1975, pp. 503–515.
[10] I.J. Beyerlein, L. Capolungo, P.E. Marshall, R.J. McCabe, C.N. Tome, Statistical analyses of deformation twinning in magnesium, Philos. Mag. 90 (2010) 2161–2190.
[11] D.W. Brown, S.R. Agnew, M.A.M. Bourke, T.M. Holden, S.C. Vogel, C.N. Tomé, Internal strain and texture evolution during deformation twinning in magnesium, Mater. Sci. Eng. A 399 (2005) 1–12, http://dx.doi.org/10.1016/j.msea.2005.02.016.
[12] S. Godet, L. Jiang, A. Luo, J. Jonas, Use of Schmid factors to select extension twin variants in extruded magnesium alloy tubes, Scr. Mater. 55 (2006) 1055–1058, http://dx.doi.org/10.1016/j.scriptamat.2006.07.059.
[13] S.H. Park, S.-G. Hong, C.S. Lee, Activation mode dependent {10–12} twinning characteristics in a polycrystalline magnesium alloy, Scr. Mater. 62 (2010) 202–205, http://dx.doi.org/10.1016/j.scriptamat.2009.10.027.
[14] M.R. Barnett, A. Ghaderi, J. Quinta da Fonseca, J.D. Robson, Influence of orientation on twin nucleation and growth at low strains in a magnesium alloy, Acta Mater. 80 (2014) 380–391, http://dx.doi.org/10.1016/j.actamat.2014.07.013.
[15] L. Capolungo, P.E. Marshall, R.J. McCabe, I.J. Beyerlein, C.N. Tomé, Nucleation and growth of twins in Zr: a statistical study, Acta Mater. 57 (2009) 6047–6056, http://dx.doi.org/10.1016/j.actamat.2009.08.030.
[16] J.J. Jonas, S. Mu, T. Al-Samman, G. Gottstein, L. Jiang, È. Martin, the role of strain accommodation during the variant selection of primary twins in magnesium, Acta Mater. 59 (2011) 2046–2056, http://dx.doi.org/10.1016/j.actamat.2010.12.005.
[17] M.R. Barnett, Z. Keshavarz, A.G. Beer, X. Ma, Non-Schmid behaviour during secondary twinning in a polycrystalline magnesium alloy, Acta Mater. 56 (2008) 5–15, http://dx.doi.org/10.1016/j.actamat.2007.08.034.
[18] U. Lienert, M.C. Brandes, J.V. Bernier, J. Weiss, S.D. Shastri, M.J. Mills, M.P. Miller, In situ single-grain peak profile measurements on Ti–7Al during tensile deformation, Mater. Sci. Eng. A 524 (2009) 46–54, http://dx.doi.org/

10.1016/j.msea.2009.06.047.
[19] H.F. Poulsen, S.F. Nielsen, E.M. Lauridsen, S. Schmidt, R.M. Suter, U. Lienert, L. Margulies, T. Lorentzen, D. Juul Jensen, Three-dimensional maps of grain boundaries and the stress state of individual grains in polycrystals and powders, J. Appl. Crystallogr. 34 (2001) 751–756, http://dx.doi.org/10.1107/S0021889801014273.
[20] B.C. Larson, W. Yang, G.E. Ice, J.D. Budai, J.Z. Tischler, Three-dimensional X-ray structural microscopy with submicrometer resolution, Nature 415 (2002) 887–890.
[21] F. Hofmann, B. Abbey, L. Connor, N. Baimpas, X. Song, S. Keegan, K. Alexander, Imaging of grain-level orientation and strain in thicker metallic polycrystals by high energy transmission micro-beam Laue (HETL) diffraction techniques, Int. J. Mater. Res. 103 (2012) 192–199.
[22] A.J. Wilkinson, G. Meaden, D.J. Dingley, Mapping strains using electron backscatter diffraction. Electron Backscatter Diffr. Mater. Sci., 2009, ISBN 978-0-387-88136-2.
[23] T.B. Britton, A.J. Wilkinson, High resolution electron backscatter measurements of elastic variations in the presence of large lattice rotations, Ultramicroscopy 114 (2012) 82–95.
[24] L. Wang, J. Lind, H. Phukan, P. Kenesei, J.-S. Park, R.M. Suter, A.J. Beaudoin, T.R. Bieler, Mechanical twinning and detwinning in pure Ti during loading and unloading – an in situ high-energy X-ray diffraction microscopy study, Scr. Mater. 92 (2014) 35–38, http://dx.doi.org/10.1016/j.scriptamat.2014.08.008.
[25] H. Abdolvand, M. Majkut, J. Oddershede, S. Schmidt, U. Lienert, B.J. Diak, P.J. Withers, M.R. Daymond, On the deformation twinning of Mg AZ31B: a three-dimensional synchrotron X-ray diffraction experiment and crystal plasticity finite element model, Int. J. Plast. 70 (2015) 77–97, http://dx.doi.org/10.1016/j.ijplas.2015.03.001.
[26] H. Abdolvand, M.R. Daymond, Multi-scale modeling and experimental study of twin inception and propagation in hexagonal close-packed materials using a crystal plasticity finite element approach—Part I: average behavior, J. Mech. Phys. Solids 61 (2013) 783–802, http://dx.doi.org/10.1016/j.jmps.2012.10.013.
[27] H. Abdolvand, M.R. Daymond, Multi-scale modeling and experimental study of twin inception and propagation in hexagonal close-packed materials using a crystal plasticity finite element approach; part II: local behavior, J. Mech. Phys. Solids 61 (2013) 803–818, http://dx.doi.org/10.1016/j.jmps.2012.10.017.
[28] H. Qin, J.J. Jonas, H. Yu, N. Brodusch, R. Gauvin, X. Zhang, Initiation and accomodation of primary twins in high-purity titanium, Acta Mater. 71 (2014) 293–305.
[29] S. Wang, C. Schuman, L. Bao, J.S. Lecomte, Y. Zhang, J.M. Raulot, M.J. Philippe, X. Zhao, C. Esling, Variant selection criterion for twin variants in titanium alloys deformed by rolling, Acta Mater. 60 (2012) 3912–3919.
[30] M.H. Yoo, Interaction of slip dislocations with twins in hcp metals, Trans. Met. Soc. AIME1 245 (1969) 2015–2060.
[31] P.A. Juan, S. Berbenni, M.R. Barnett, C.N. Tome, L. Capolungo, A double inclusion homogenization scheme for polycrystals with hierarchal topologies: application to twinning in Mg alloys, Int. J. Plast. 60 (2014) 182–196.
[32] T.B. Britton, A.J. Wilkinson, Measurement of residual elastic strain and lattice rotations with high reoslution electron backscatter diffraction, Ultramicroscopy 111 (2011) 1395–1404.
[33] D.J. Dingley, A.J. Wilkinson, G. Meaden, P.S. Karamched, Elastic strain tensor measurement using electron backscatter diffraction in the SEM, J. Electron Microsc. Tokyo 59 (Supple) (2010) 155–163.
[34] E.S. Fisher, C.J. Renken, Single crystal elastic moduli and the hcp to bcc transformation in Ti, Zr, and Hf, Phys. Rev. 135 (1964).
[35] T. Benjamin Britton, A.J. Wilkinson, Stress fields and geometrically necessary dislocation density distributions near the head of a blocked slip band, Acta Mater. 60 (2012) 5773–5782, http://dx.doi.org/10.1016/j.actamat.2012.07.004.
[36] J.F. Nye, Some geometrical relations in dislocated crystals, Acta Met. 1 (1953) 153–162.
[37] I.P. Jones, W.B. Hutchinson, Stress state dependence of slip in Ti64 and other HCP metals, Acta Met. 29 (1981) 951–968.
[38] A.J. Wilkinson, G. Meaden, D.J. Dingley, High-resolution elastic strain measurement from electron backscatter diffraction pattern: new level of sensitivity, Ultramicroscopy 106 (2006) 307–313.
[39] T.B. Britton, J. Jiang, Y. Guo, A. Vilalta-Clemente, D. Wallis, L.N. Hansen, A. Winkelmann, A.J. Wilkinson, Tutorial: crystal orientations and EBSD — or which way is up? Mater. Charact. 117 (2016) 113–126, http://dx.doi.org/10.1016/j.matchar.2016.04.008.
[40] H. Abdolvand, A.J. Wilkinson, On the effects of reorientation and shear transfer during twin formation: comparison between high resolution electron backscatter diffraction experiments and a crystal plasticity finite element model, Int. J. Plast. (2016) 1–23, http://dx.doi.org/10.1016/j.ijplas.2016.05.006.
[41] R.J. Asaro, A. Needleman, Flow localization in strain hardening crystalline solids, Scr. Matallurgica. 18 (1984) 429–435.
[42] X. Wu, S.R. Kalidindi, C. Necker, A.A. Salem, Prediction of crystallographic texture evolution and anisotropic stress-strain curves during large plastic strains in high purity ??-titanium using a Taylor-type crystal plasticity model, Acta Mater. 55 (2007) 423–432, http://dx.doi.org/10.1016/j.actamat.2006.08.034.
[43] J. Gong, A.J. Wilkinson, A microcantilever investigation of size effect, solid-solution strengthening and second-phase strengthening for ⟨a⟩ prism slip in alpha-Ti, Acta Mater. 59 (2011) 5970–5981, http://dx.doi.org/10.1016/j.actamat.2011.06.005.
[44] A. Akhtar, Basal slip and twinning in a-titanium single crystals, Metall. Mater. Trans. A 6 (1975) 1105–1113.
[45] M.A. Kumar, A.K. Kanjarla, S.R. Niezgoda, R.A. Lebensohn, C.N. Tome, Numerical study of the stress state of a deformation twin in magnesium, Acta Mater. 84 (2015) 349–358.
[46] Z. Jin, T.R. Bieler, An in-situ obervation of mechanical twin nucleation and propagation in TiAl, Philos. Mag. A 71 (1995) 925–947.